

Ultrasonic image artifact removal technique based on SoS kernel

Song Shoupeng Jia Hui Chen Dan

(School of Mechanical Engineering, Jiangsu University, Zhenjiang 212013, China)

Abstract: To solve the problem of heavy artifacts in ultrasonic images, a novel ultrasonic imaging method is presented using a sum of sinc (SoS) kernel for eliminating the artifacts caused by the diffusion of isacoustic path, signal tail, or noise simultaneously. First, the envelope of ultrasonic echo is obtained and passed through a SoS kernel, then the signal is sampled at equal intervals determined by the echo signal information degree, and the Fourier transform is applied to the discrete sampling data to obtain the Fourier coefficient sequence. After that, the spectral estimation algorithm is used to estimate the parameters of the ultrasonic echo signal and reconstruct the echo signal using the estimated parameters. Finally, the ultrasonic image is obtained by calculating the acoustic field using the reconstructed echoes. Experimental results show that the image artifacts are effectively removed using focused and straight probes to test straight slot defects and through-hole defects, respectively. Compared with the B-scan images, the peak signal-to-noise ratios reach 24.306, 23.213, 15.074, and 16.444 dB, and the structural similarity indexes are 0.931, 0.932, 0.746, and 0.773, which indicates that the quality of the defect images is greatly improved using the proposed method.

Key words: nondestructive testing; ultrasonic image; artifact; sum of sinc (SoS) kernel; defect

DOI: 10.3969/j.issn.1003-7985.2024.01.009

Industrial ultrasonic images serve as visual representations of testing data derived from an ultrasonic transducer. These images enable direct observation of the location, shape, and size of the defects^[1-3]. Generally, ultrasonic images are formed from the spatial acoustic intensity calculated from the testing data. There are several types of imaging methods, such as B-scan, C-scan, phased array, synthetic aperture, full matrix capture, and total focus method^[4-5]. However, these methods share a common drawback: image quality is often reduced owing to artifacts and noise^[6-7]. Furthermore, these artifacts may lead to inaccuracies in defect evaluation.

To eliminate image artifacts, researchers have devel-

oped different techniques. These can be divided into pre-processing and postprocessing methods. Preprocessing methods focus on removing noise from acquisition data or improving the imaging algorithm to prevent artifacts. Postprocessing methods aim to reduce artifacts already present in the image using various algorithms. Generally, artifacts are generated by the diffusion of the isacoustic path, signal tail, and noise. In 2016, Chen^[8] proposed setting an intensity threshold to identify artifacts, which were then filled with the weighted average values from surrounding pixels. Others have suggested using the acoustic field directivity function to correct the energy attenuation coefficient, thereby reducing image artifacts^[9-10]. In 2022, Song and Chen^[11] identified defective images and artifacts based on the number of effective intersections of the isacoustic path, then filled the artifact area with the minimum intensity pixel value of the image. The signal tail, also known as the echo trailing phenomenon, has been addressed by He and Fang^[12], who designed a circuit in 2005 to change the circuit dampness to reduce the echo signal tail according to the circuit equivalent model. Iakovleva et al.^[13] proposed a parametric and weighted filtering technique to reduce the high-amplitude artifacts caused by the bottom reflection of the test piece. In 2018, Sy et al.^[14] proposed two methods to filter artifacts in the total focusing method, while Yang et al.^[15] used a discrete wavelet transform to filter signals and reduce artifacts caused by imaging background noise. Moreover, Potter et al.^[16] proposed a technique to reduce artifacts using a hybrid full matrix formed through a temporally weighted sum of coherent and reconstructed matrices. In addition, Zhang et al.^[17] proposed a method that combined weighting function filtering and a truncation imaging algorithm to eliminate artifacts. Budyn^[18] adopted a statistical robustness geometry mid-value to replace the delay-superposition imaging algorithm for artifact suppression. In 2019, Zheng et al.^[19] generated a phase reversal signal to counteract the signal tail.

This study proposes a new method for the removal of ultrasonic image artifacts, utilizing the sum of sinc (SoS) kernel. This method effectively eliminates different types of artifacts in ultrasound images while retaining essential information regarding the location, shape, and size of defects. In this process, we first receive the ultrasonic echo signal and allow it to pass through a modulation function known as the SoS kernel. Subsequently, we perform sparse sampling on the modulated signal at uniform inter-

Received 2023-10-12, **Revised** 2023-12-25.

Biography: Song Shoupeng (1967—), male, doctor, professor, songshoupeng@126.com.

Foundation item: The National Natural Science Foundation of China (No. 52175511).

Citation: Song Shoupeng, Jia Hui, Chen Dan. Ultrasonic image artifact removal technique based on SoS kernel[J]. Journal of Southeast University (English Edition), 2024, 40(1): 80 – 88. DOI: 10.3969/j.issn.1003-7985.2024.01.009.

vals, which are determined by the degree of information contained within the echo signal. Next, we calculate the Fourier coefficients of the echo signal and use the spectrum estimation algorithm to estimate the echo parameters. Finally, we reconstruct the echo and use this reconstructed signal to plot the defect ultrasonic image, thereby producing an ultrasonic image. In the following section, we first describe the causes of ultrasonic artifacts. Then, we present the principle of ultrasonic imaging based on the SoS kernel. Finally, we conduct experiments on a test sample using different transducers and defects. The experimental results indicate that the number of artifacts is greatly reduced compared with other ultrasonic imaging methods.

1 Causes of the Formation of Ultrasound Image Artifacts

Artifacts in industrial ultrasound images are nontarget images formed by both inherent and random errors. These artifacts can potentially lead to false evaluation results of defects. There are primarily three causes for the formation of image artifacts. The first cause is inherent error induced by the algorithm used to calculate the spatial acoustic field of the test sample, often referred to as the isacoustic path. The second cause is attributed to the phenomenon of ultrasonic echo signal trailing, a type of random error. This occurs when the received echo signal continues to resonate, causing the echo to persist with non-zero amplitudes. The third cause of artifact formation is random noise, which blurs the image.

In industrial ultrasonic testing, an ultrasonic signal is generated by an electrical pulse exciting a piezoelectric transducer. Suppose the ultrasonic echo signal $x_{ij}(t)$ can be characterized by the following mathematical model^[20]:

$$x_{ij}(t) = \sum_{k=1}^K a_k g_0(t - t_k) \cos(2\pi f_0(t - t_k) + \varphi_k) + \varepsilon(t) \quad (1)$$

where i represents the emission transducer, j represents the receiving transducer; $g_0(t) = \exp[-(t/\eta)^2]$, η is the pulse width factor of the echo signal; f_0 is the center frequency of the transducer; K denotes the number of pulse echoes; φ_k is the initial phase; a_k and t_k are the echo peak amplitude and time delay, respectively, $\{t_k, a_k\}_{k=1}^K$, $t_k \in [0, \tau)$, $a_k \in \mathbf{R}$; $\varepsilon(t)$ denotes the random noise.

Ultrasonic imaging calculates the sound field distribution of the test sample using the sound intensity obtained from the echo signal. This is achieved using the delay and superposition rule to form a spatial acoustic field distribution map from multiple sensor echo signals. If the acoustic intensity $\text{INT}(x_p, y_p)$ is presented using different colors, an ultrasonic color image is generated, which can be expressed as follows:

$$\text{INT}(x_p, y_p) = \sum_{i=1}^N \sum_{j=1}^M x_{ij}(t_{ij}(x_p, y_p)) \quad (2)$$

where N is the number of emission transducers; M is the number of receiving transducers; $t_{ij}(x_p, y_p)$ represents the time of flight at a spatial point (x_p, y_p) .

An isacoustic path is formed when the sum of the emission beam path and the receiving beam path are equal. However, since the spatial points with equal isacoustic paths are not unique, image artifacts can be generated.

The oscillation duration of echo $x_{ij}(t)$ differs depending on the pulse width factor η , resulting in a nonzero duration of sound intensity, resulting in a nonzero duration of sound intensity. This can lead to the production of trailing artifacts, which can extend and blur the edge of the image randomly. Meanwhile, the presence of noise $\varepsilon(t)$ will also influence the ultrasonic image randomly. Therefore, these three factors can create artifacts in ultrasound images.

2 Ultrasonic Imaging Technique Based on the SoS Kernel

The SoS kernel refers to the sum of sinc functions with weighted coefficients. Its time-domain formula can be expressed as^[21]

$$s(t) = \text{rect}\left(\frac{t}{\pi}\right) \sum_{m \in \Psi} c_m \exp\left(j \frac{2\pi m t}{\tau}\right) \quad (3)$$

where τ is the signal duration; Ψ denotes a continuous set of integers with the length of the set number divided by the number of signal echoes; c_m denotes a weighted coefficient satisfying $\forall m \in \Psi$ and $c_m \neq 0$. The waveform $s(t)$ is determined by $\{c_m\}_{m \in \Psi}$, and the time-frequency response of the SoS kernel changes according to $\{c_m\}_{m \in \Psi}$, which can lead to different modulation results.

By transforming the time-domain expression of $s(t)$ to frequency-domain expression $S(\omega)$, we have

$$S(\omega) = \frac{\tau}{\sqrt{2\pi}} \sum_{m \in \Psi} c_m \text{sinc}\left(\frac{\omega}{2\pi/\tau} - m\right) \quad (4)$$

The time-domain and frequency-domain waveforms of the SoS kernel are shown in Figs. 1(a) and (b), respectively, with the exception of all weighted coefficients c_m that are 1.

Let the ultrasonic echo $x(t)$ pass through the kernel, which is equivalent to the time domain convolution with $s(t)$. The output signal $y(t)$ can be obtained as

$$y(t) = x(t)s(t) = \int_{-\infty}^{\infty} x(\tau)s(t - \tau)d\tau \quad (5)$$

Then, by sampling the modulated signal $y(t)$ with equal interval T , a discrete sequence $y(m)$ can be obtained. Here, the sampling interval T is not satisfied by the Nyquist sampling rule, which is larger than the

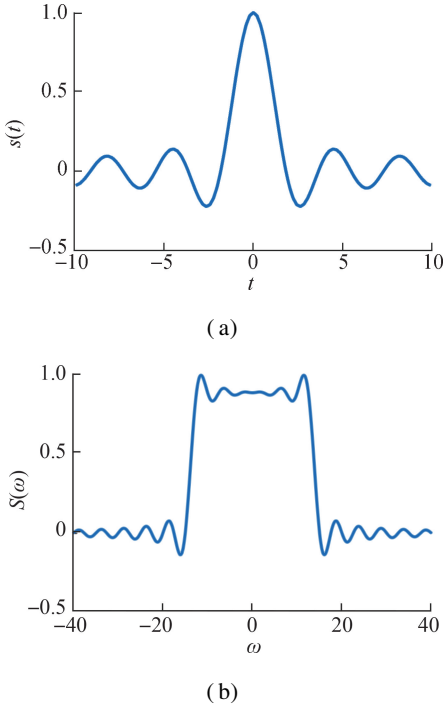


Fig. 1 Example waveform of the SoS kernel. (a) Time domain; (b) Frequency domain

Nyquist sampling interval. Meanwhile, the number of acquisition data is considerably less than that of the Nyquist rule.

During the data sampling procedure, the sampling interval T is determined by the degree of information within the signal over a signal duration τ . Assuming the pulse number is K , the information freedom of the signal Ω within the time τ can be calculated as follows:

$$\Omega = 2K \quad (6)$$

The number of sampling points M is

$$M = \Omega + 1 \quad (7)$$

Then, the sampling interval T is determined as

$$T = \frac{\tau}{M} \quad (8)$$

The reciprocal of the sampling interval T is the sampling frequency, which is independent of the echo signal frequency and is much lower than the Nyquist sampling frequency.

Let each peak in the echo have two degrees of information freedom: peak amplitude and time delay. Then the number of sampling points M_u of the echo with the sampling period τ should be

$$M_u = 2K + 1 \quad (9)$$

In general, the echo parameters can be uniquely determined by the sampling points M_u . However, larger M_u is often adopted to improve the accuracy of the solution.

Suppose the echo can be determined by the signal information freedom, peak amplitude, and time delay, then the sampling discrete sequence $y(m)$ can be rewritten as follows by the Dirac function $\delta(t)$ ^[22]:

$$y(m) = \sum_{m \in \mathbf{Z}} \sum_{k=1}^K a_k \delta(t - t_k - m\tau) \quad (10)$$

where $\delta(t)$ denotes the unit impulse function.

Taking the discrete Fourier transform (DFT) on the discrete sampling sequence $y(m)$, the Fourier coefficients $Y[m]$ can be obtained as follows:

$$Y[m] = \frac{1}{\tau} \sum_{k=1}^{K-1} \alpha_k \left[\exp\left(-j \frac{2\pi t_k}{\tau}\right) \right]^m \quad (11)$$

The Fourier coefficients $Y[m]$ contain information on the time delay t_k and amplitude α_k of the original signal $x(t)$.

Using the annihilating filter method^[23] to estimate the parameters $\{t_k, \alpha_k\}_{k=1}^K$, an annihilating filter needs to be constructed with coefficients $\{h(m)\}_{m=0}^K$.

Let $Y[m] = \frac{1}{\tau} C[m]$, where $m \in \mathbf{Z}$, and its Z transformation can be expressed as follows:

$$H(z) = \sum_{m=0}^K h(m) z^{-m} \quad (12)$$

Suppose the zero points of $H(z)$ are $\beta_k = \exp\left(-j \frac{2\pi}{\tau} t_k\right)$, and let $h(0) = 1$, then $H(z)$ can be further expressed as follows with factorization:

$$H(z) = \prod_{k=0}^{K-1} (1 - \alpha_k z^{-1}) \quad (13)$$

Assuming all time delays $\{t_k\}_{k=1}^K$ are unequal, the zero points of the filter can uniquely express the time delay $\{t_k\}_{k=1}^K$. If the coefficients $h(m)$ of the annihilating filter can be obtained, the parameters $\{a_k\}_{k=1}^K$ can be calculated from $H(z)$; furthermore, the $\{t_k\}_{k=1}^K$ can be estimated. The procedure to solve this can be described as follows.

Let the filter coefficients $h(m)$ be convolved with $C[m]$. If the Z-transform of the annihilating filter satisfies $H(\beta_k) = 0$, the convolution results will be zero. This allows us to calculate the filter coefficients $h(m)$, which can be expressed as follows:

$$h(m) C[m] = \sum_{\gamma=0}^K h(\gamma) C[m - \gamma] = 0 \quad (14)$$

Let $h(0) = 1$ and expand it as follows:

$$h(1) C[m - 1] + h(2) C[m - 2] + \dots + h(K) C[m - K] = -C[m] \quad (15)$$

In Eq. (15), K unknown parameters $\{h(1), h(2), \dots, h(K)\}$ can be calculated from K equations, which require at least $2K$ Fourier series coefficients. Generally, the

number of Fourier series coefficients L and the echo peaks K satisfy the following equation^[24]:

$$L = 2l + 1 \geq 2K \quad (16)$$

Then, $\{t_k, a_k\}_{k=1}^K$ can be estimated.

According to $\{t_k, a_k\}_{k=1}^K$, a signal $\hat{x}(t)$ can be recon-

structed if the peak envelope is a Gaussian function. Taking the signal $\hat{x}(t)$ as an approximation signal of $x(t)$ and calculating the sound field intensity $\text{INT}(x_p, y_p)$ of the test sample, an ultrasonic image will be presented using a chromaticity scale. The imaging process is illustrated in Fig. 2.

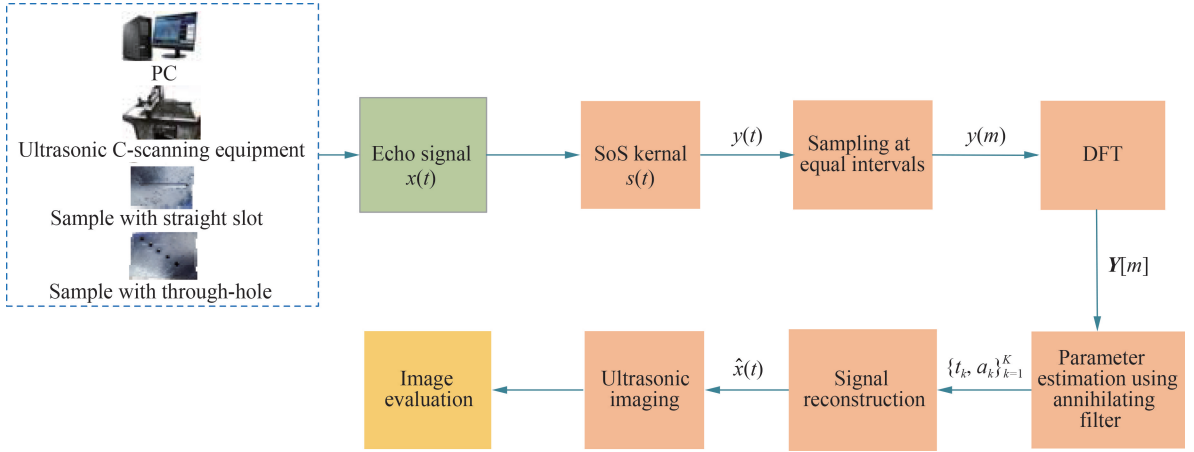


Fig. 2 Ultrasonic imaging procedure

3 Analysis of the Experiments and Results

To verify the effectiveness of the proposed imaging method, we conducted defect testing experiments using ultrasonic C-scanning equipment (type: BSN-C3024). The system comprises an ultrasonic transducer, T/R circuits,

and a data acquisition system. The test system platform is shown in Fig. 3. The aluminum specimens were fabricated with two types of defects: straight slots and through holes. The through holes are numbered as 1[#], 2[#], 3[#], 4[#] and 5[#] with same diameter of 2 mm. The geometric distribution of the defects is shown in Fig. 4.

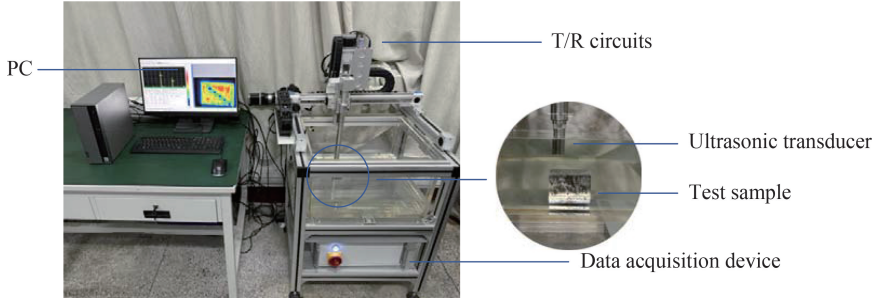


Fig. 3 Inspection system platform

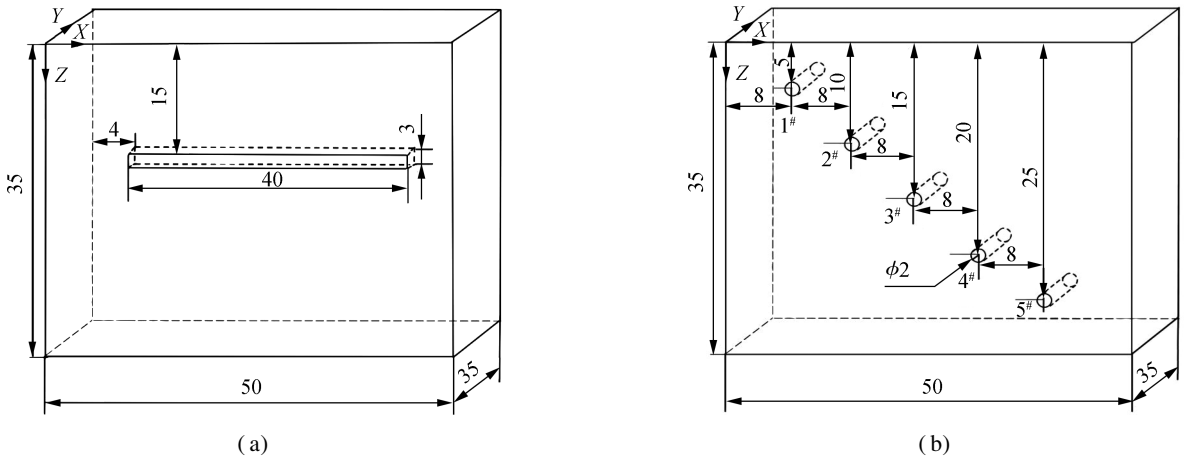


Fig. 4 Diagram of defects (unit: mm). (a) Straight slot; (b) Through hole

3.1 Focusing the transducer testing experiment

An immersion-focused transducer identified as I2-5P13F75-H (1GI1292) was used for testing, with a central frequency of 5 MHz and an active element diameter of 13 mm. Its focal length in water is 78 mm. We positioned the transducer in water, maintaining a lift-off of 15 mm above the top surface of the sample, with the focal point centered within the sample.

The received signal was amplified with a gain of 25 dB filtered with a bandwidth of 2-6 MHz. Subsequently, the signal envelope was extracted to obtain $x(t)$. The ultrasonic echo signal $x(t)$ was modulated by the SoS kernel to obtain $y(t)$, and the discrete signal sampling sequence value $y(m)$ was sampled at equal intervals T from $y(t)$. In the experiments, the signal sampling duration τ was 11.1 μs , the number K was 2, and the information degree of freedom Ω was 4. The number of sampling points is 198, and the sampling interval T is 0.056 μs .

After deriving the Fourier coefficients $Y[m]$ from the sampling sequence $y(m)$, we used the annihilating filter method to estimate the parameter $\{t_k, a_k\}_{k=1}^K$, resulting in the reconstructed echo signal $\hat{x}(t)$. Figs. 5(a) and (b) display an example of the time-domain waveforms of signals $x(t)$ and $\hat{x}(t)$.

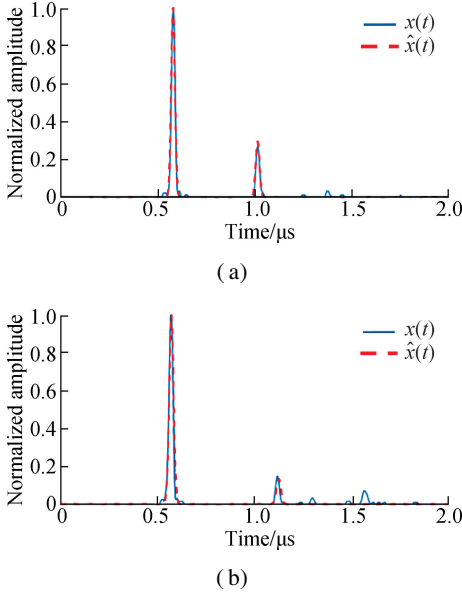


Fig. 5 Received and reconstructed signals of two defect types with a focusing probe. (a) Straight slot; (b) Through hole

Fig. 6(a) depicts the ultrasound image of the straight slot defect obtained using the B-scan imaging method. Fig. 6(b) shows the ultrasound image of the same defect type obtained using the proposed method. In addition, Fig. 7(a) represents the ultrasonic images of through-hole defects obtained using the B-scan imaging method, while Fig. 7(b) shows the ultrasonic images of the same defect type obtained using the proposed method.

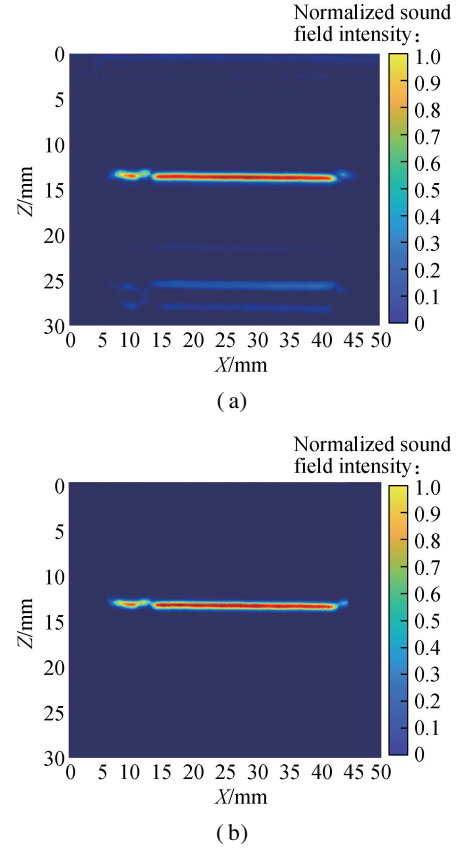


Fig. 6 Ultrasound images of straight slot defects with a focusing probe. (a) B-scan image method; (b) Proposed image method

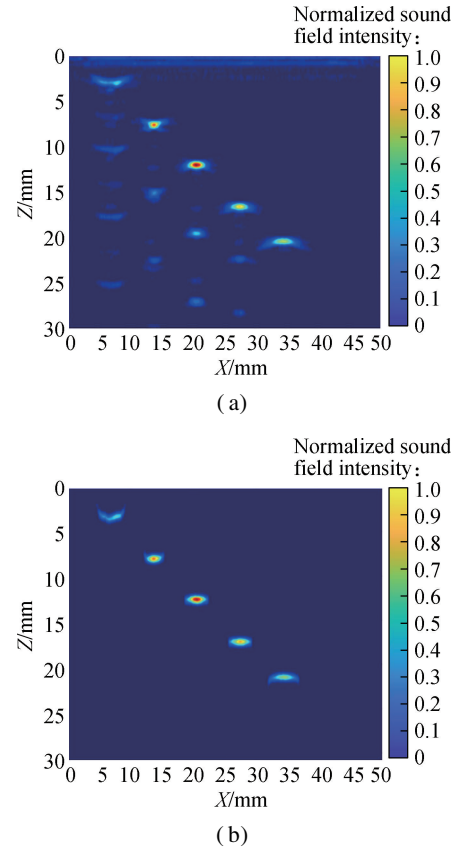


Fig. 7 Ultrasonic images of through-hole defects with a focusing probe. (a) B-scan image method; (b) Proposed image method

In Figs. 6(a) and 7(a), the artifacts are clearly presented. However, these are significantly reduced in Figs. 6(b) and 7(b), resulting in images clearer for observation and evaluation.

The actual size of the straight slot defect on the sample is 40 mm × 3 mm in the xoz plane. When estimated with a 6 dB maximum amplitude in the image region, the size of the same defect is 37.44 mm × 2.23 mm according to Fig. 6(a) and 37.61 mm × 2.34 mm according to Fig. 6(b). The relative error of the straight slot defect distribution area is 30.8%, owing to artifacts. After removing the artifacts, the relative error decreased to 26.78%, showing an improvement of 4.02%.

Each through-hole defect has an actual area of 3.14 mm² in the xoz plane. The measured mean area of the through-hole defect in the 6 dB image, as shown in Fig. 7(a), is 2.298 mm² with a relative error of 26.4%. After removing the artifacts, the measured mean area increased to 2.406 mm², as shown in Fig. 7(b), and the relative error reduced to 23.3%, making an improvement of 3.1%.

The relative error ΔH can be calculated using the following formula^[11]:

$$\Delta H = \frac{|a' - a|}{a} \times 100\% \quad (17)$$

where a is the actual area of the defect; a' represents the measured area from the image with a 6 dB amplitude.

3.2 Straight transducer testing experiment

Another straight ultrasonic transducer, I2-5P13-H (1GI0736), was used to detect the same defects with a center frequency of 5 MHz and a sensitive element diameter of 13 mm. The lift-off was 12 mm from the sample top surface in water.

The received signal was amplified with a gain of 32 dB and filtered within a 2-6 MHz bandwidth. The signal envelope was subsequently extracted to obtain $x(t)$. The signal was modulated by the SoS kernel to derive signal $y(t)$. The discrete sampling sequence $y(m)$ was obtained by sampling $y(t)$ with a uniform interval T . In the experiment, the signal duration τ was 8.96 μ s, the number K was 3, and the information degree of freedom Ω was 6. The number of sampling points was 160 at a sampling interval T of 0.056 μ s. Adopting the same procedures as in the first experiment, we were able to generate a defective ultrasonic image. Figs. 8(a) and (b) illustrate examples of the received signal $x(t)$ and the reconstructed signal $\hat{x}(t)$ obtained from two types of defects, respectively.

Fig. 9(a) illustrates the ultrasound image of a straight slot defect captured using the B-scan imaging method. By contrast, Fig. 9(b) shows the ultrasound image of the same defect type obtained using the proposed method.

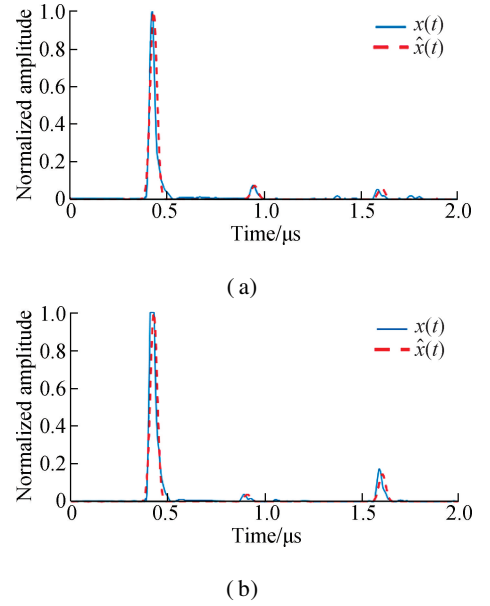


Fig. 8 Received and reconstructed signals of two defect types with a straight probe. (a) Straight slot; (b) Through hole

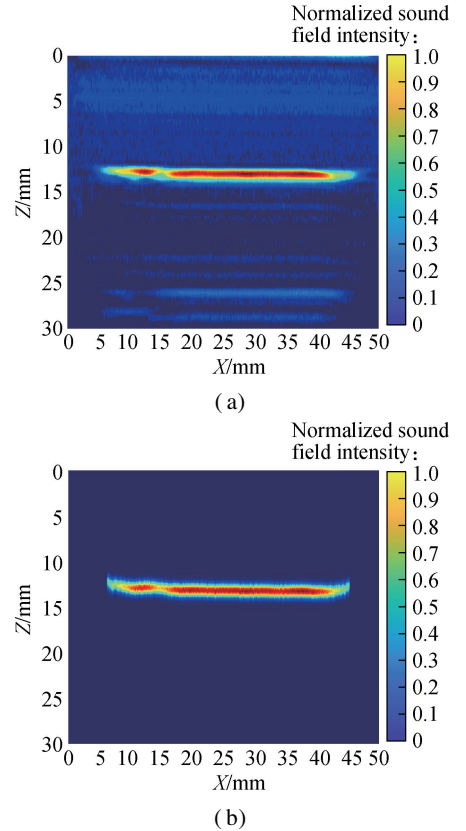


Fig. 9 Ultrasonic images of a straight slot defect with a straight probe. (a) B-scan image; (b) Proposed image method

Similarly, Fig. 10(a) illustrates the ultrasonic images of through-hole defects as obtained by the B-scan imaging method, while Fig. 10(b) indicates the ultrasonic images of the same defect type obtained using the proposed method.

Artifacts resulting from isacoustic path signal trailing and noise are evident in Figs. 9(a) and 10(a). However, these artifacts are largely suppressed in Figs. 9(b) and 10(b).

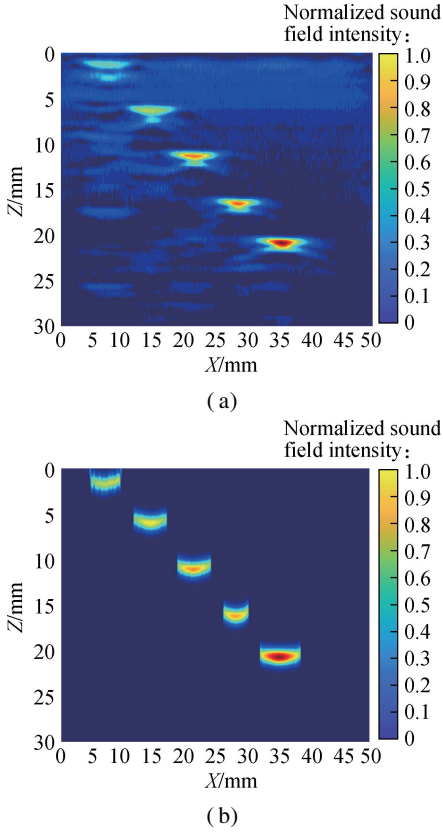


Fig. 10 Ultrasonic images of a through-hole defect with a straight probe. (a) B-scan image; (b) Proposed image method

The estimated size of the through-hole defect is 35.1 mm × 2.16 mm in Fig. 9(a) and 36.1 mm × 2.36 mm in Fig. 9(b). Initially, the relative error was 36.8% owing to artifacts. After removing the artifacts, the relative error was reduced to 29%, marking an improvement of 7.8%.

The measured mean area of the through-hole defect, with artifacts, is 2.196 mm², as shown in Fig. 10(a), with a relative error of 30.1%. After removing the artifacts, the measured mean area increased to 2.436 mm², as shown in Fig. 10(b), with a relative error of 22.4%, which increased by 7.7%.

To evaluate the quality of the images produced by the two imaging methods, we introduce objective indexes, such as the mean squared error (MSE), peak signal-to-noise ratio (PSNR), and structural similarity index (SSIM).

MSE evaluates the pixel-level difference between two images. In this case, one image is the B-scan image with artifacts, and the other is the image with artifacts removed using our proposed method. A smaller MSE indicates greater similarity between the images.

Assuming that the image pixel is $U \times V$, and the sum of the pixel number is E , the MSE can be calculated by^[25]

$$\zeta = \frac{1}{UV} \sum_{I=0}^U \sum_{J=0}^V [f(X_I, Y_J) - f'(X_I, Y_J)]^2 \quad (18)$$

where ζ indicates MSE; X is the B-scan image; $f(X_I, Y_J)$

is the image pixel value derived using B-scan imaging; f' is the image of the proposed method; $f'(X_I, Y_J)$ is the image pixel value derived using the proposed method.

PSNR is a classic objective evaluation indicator that represents the ratio of the maximum signal power in the current image to noise, which characterizes the quality of the processed image. The calculation formula is^[25]

$$\text{PSNR} = 10 \lg \left(\frac{(2^b - 1)^2}{\zeta} \right) \quad (19)$$

where b is the number of bits per pixel. The specific value of PSNR is inversely proportional to the degree of distortion of the fused image. In other words, the larger the value, the smaller the distortion.

SSIM considers the brightness, structure, and contrast of the image and can be calculated using the following formula^[25]:

$$\text{SSIM}(X, Y) = \frac{(2\mu_X\mu_Y + C_1)(2\sigma_{XY} + C_2)}{(\mu_X^2 + \mu_Y^2 + C_1)(\sigma_X^2 + \sigma_Y^2 + C_2)} \quad (20)$$

where C_1 and C_2 are all constants; μ_X and μ_Y represent the average brightness of the images before and after processing, respectively; σ_X and σ_Y indicate the standard deviation of the images before and after processing, respectively; σ_{XY} is the variance between the two compared images.

$$\left. \begin{aligned} \mu_X &= \frac{1}{E} \sum_I^E X_I \\ \mu_Y &= \frac{1}{E} \sum_I^E Y_I \\ \sigma_X &= \sqrt{\frac{1}{E-1} \sum_I^E (X_I - \mu_X)^2} \\ \sigma_Y &= \sqrt{\frac{1}{E-1} \sum_I^E (Y_I - \mu_Y)^2} \\ \sigma_{XY} &= \frac{1}{E-1} \sum_I^E (X_I - \mu_X)(Y_I - \mu_Y) \end{aligned} \right\} \quad (21)$$

The evaluation results of the images are shown in Table 1. The value of MSE indicates the image noise level. The MSE values in Figs. 6, 7, 8, and 9 are 241.252, 310.276, 1 474.581, and 2 021.332, respectively, when compared to those derived using the B-scan images. Given the higher noise content in B-scan images, their quality is lower than that of images produced using our proposed method. The MSE values in Figs. 9 and 10 are higher than those in Figs. 6 and 7. This suggests that the straight probe introduces more noise than the focusing probe. Furthermore, PSNR measures the degree of image distortion. A larger PSNR value indicates lower distortion and fewer artifacts. The PSNR values in Figs. 6, 7, 8, and 9 are 24.306, 23.213, 15.074, and 16.444 dB, respectively. The PSNR values in Figs. 6 and 7 are larger than those in Figs. 9 and 10. Moreover, SSIM

reflects the similarity between images. A higher SSIM value indicates that the images obtained using the proposed image method retain more defect information. The SSIM values in Figs. 6, 7, 8, and 9 are 0.931, 0.932, 0.746, and 0.773, respectively. The SSIM values in Figs. 6 and 7 are closer to 1 than those in Figs. 9 and 10. Overall, the results of the objective indexes show that the proposed imaging method effectively removes artifacts and retains defective key information.

Table 1 Evaluation index results of the ultrasonic image

Probe type	Defect type	MSE	PSNR/dB	SSIM
Focusing probe	Straight slot	241.252	24.306	0.931
	Through-hole	310.276	23.213	0.932
Straight probe	Straight slot	1 474.581	15.074	0.746
	Through-hole	2 021.332	16.444	0.773

4 Conclusions

1) We analyze the causes of artifact generation in ultrasound imaging and proposed an ultrasound imaging method based on SoS kernel modulation. This method involves modulating the echo signal through convolution. The sampling pattern of the signal is determined by key imaging parameters in the echo signal, specifically the echo peak time delay and amplitude. The parameters are estimated from the sampled data using the annihilating filter algorithm. Subsequently, the echo signal is reconstructed using these parameters. Finally, we use the reconstructed echo signal for ultrasonic imaging, which produces an ultrasonic image of the defect with significantly reduced artifacts.

2) To verify the effectiveness of the proposed imaging method, we construct a testing system. Two types of ultrasonic transducers (i.e., point focusing probe and straight probe) are used to test the straight slot defect and through-hole defect, respectively. Imaging is performed separately using the conventional B-scan imaging method and the proposed method.

3) The imaging results reveal that the proposed method can effectively reduce the artifacts caused by the diffusion of the isacoustic path, signal trailing phenomena, and noise. Improved image quality is achieved either by directly observing the defect images or calculating the objective evaluation indexes. These indexes retain important information regarding the defect location and morphology, resulting in less image distortion. When comparing B-scan images of different transducer types and defect types, the MSE values are 241.252, 310.276, 1 474.581, and 2 021.332; the PSNR values are 24.306, 23.213, 15.074 and 16.444 dB; and the SSIM values are 0.931, 0.932, 0.746, and 0.773, respectively. The experimental results also indicate that our proposed image method can provide higher-quality

images for defect quantization and evaluation.

References

[1] Li Y S, Wang L X. *Non-destructive testing personnel: Ultrasonic testing* [M]. Beijing: China Machine Press, 2013: 314 – 316. (in Chinese)

[2] Cheng J M, Gao Y Q, Yan H D, et al. Statistical analysis of nondestructive testing results of cast steel joints in civil engineering structures [J]. *Journal of Southeast University (English Edition)*, 2022, **38**(1): 1 – 8. DOI: 10.3969/j.issn.1003-7985.2022.01.001.

[3] Gan L, Jin H J, Shen Z Z. Influencing factors of characteristic parameters of digital image on concrete surface roughness [J]. *Journal of Southeast University (Natural Science Edition)*, 2022, **53**(3): 497 – 505. DOI: 10.3969/j.issn.1001-0505.2022.03.010. (in Chinese)

[4] Hoyle C, Sutcliffe M, Charlton P, et al. Ultrasonic algorithms for calculating probe separation distance, combined with full matrix capture with the total focusing method [J]. *Insight-Non-Destructive Testing and Condition Monitoring*, 2020, **62**(4): 199 – 207. DOI: 10.1784/insi.2020.62.4.199.

[5] Wang P, Liu X G, Li X T, et al. An improved measurement matrix of compressed sensing for synthetic aperture ultrasound imaging [J]. *Applied Acoustics*, 2022, **188**: 108592. DOI: 10.1016/j.apacoust.2021.108592.

[6] Wei T, Shuai L G, Zhang Y L. Influence of image data set noise on classification with a convolutional network [J]. *Journal of Southeast University (English Edition)*, 2019, **35**(1): 51 – 56. DOI: 10.3969/j.issn.1003-7985.2019.01.008.

[7] Qian Z Y, Wu H, Tang J X. Research review on intelligent methods of advanced ultrasonic technology [J]. *Non-destructive Testing Technology*, 2023, **47**(4): 1 – 5. DOI: 10.13689/j.cnki.cn21-1230/th.2023.04.003. (in Chinese)

[8] Chen S. *Research and implementation of two-dimensional ultrasound imaging system based on sparse array* [D]. Nanjing: Nanjing University of Information Science & Technology, 2016. (in Chinese)

[9] Zhou Z G, Peng D, Li Y, et al. Research on phased array ultrasonic total focusing method and its calibration [J]. *Journal of Mechanical Engineering*, 2015, **51**(10): 1 – 7. DOI: 10.3901/JME.2015.10.001. (in Chinese)

[10] Jia L C, Chen S L, Bai Z L, et al. Correction model and accelerating algorithm for ultrasonic total focusing method [J]. *Chinese Journal of Scientific Instrument*, 2017, **38**(7): 1589 – 1596. DOI: 10.19650/j.cnki.cjsi.2017.07.004. (in Chinese)

[11] Song S P, Chen Y Q. The method of eliminating isoacoustic contour artifacts in ultrasonic total focus method [J]. *Journal of Applied Acoustics*, 2022, **41**(4): 527 – 534. DOI: 10.11684/j.issn.1000-310X.2022.04.004. (in Chinese)

[12] He H L, Fang X Q. Researching on the smearing circuit of ultrasonic [J]. *Semiconductor Technology*, 2005, **30**(8): 69 – 70, 73. DOI: 10.3969/j.issn.1003-353X.2005.08.019. (in Chinese)

[13] Iakovleva E, Chatillon S, Bredif P, et al. Multi-mode

TFM imaging with artifacts filtering using CIVA UT forwards models [C]// *10th International Conference on Barkhausen and Micro-Magnetics (ICBM)*. Baltimore, MD, USA, 2014: 72 – 79. DOI: 10.1063/1.4864804.

[14] Sy K, Bredif P, Iakovleva E, et al. Development of methods for the analysis of multi-mode TFM images [J]. *Journal of Physics: Conference Series*, 2018, **1017**(1): 012005. DOI: 10.1088/1742-6596/1017/1/012005.

[15] Yang G D, Chen W, Zhan H Q, et al. Image denoising for phased array total focusing based on wavelet transform [J]. *Nondestructive Testing*, 2018, **40**(8): 53 – 56. DOI: 10.11973/wsjc201808011. (in Chinese)

[16] Potter J N, Wilcox P D, Croxford A J. Diffuse field full matrix capture for near surface ultrasonic imaging [J]. *Ultrasonics*, 2018, **82**: 44 – 48. DOI: 10.1016/j.ultras.2017.07.009.

[17] Zhang C, Huthwaite P, Lowe M. Eliminating backwall effects in the phased array imaging of near backwall defects [J]. *The Journal of the Acoustical Society of America*, 2018, **144**(2): 1075 – 1088. DOI: 10.1121/1.5051641.

[18] Budyn N. On the use of the geometric Median in delay-and-sum ultrasonic array imaging [J]. *IEEE Transactions on Ultrasonics, Ferroelectrics, and Frequency Control*, 2020, **67**(10): 2155 – 2163. DOI: 10.1109/TUFFC.2020.2993328.

[19] Zheng G R, Zhang H, Li Z, et al. Elimination of ultrasonic tailing based on the superposition method [J]. *Journal of Vibration and Shock*, 2019, **38**(2): 219 – 225. DOI: 10.13465/j.cnki.jvs.2019.02.032. (in Chinese)

[20] Yu J H. *Research on hardware implementation method of array ultrasonic signal sparse sampling based on finite rate of innovation* [D]. Zhenjiang: Jiangsu University, 2019. (in Chinese)

[21] Vetterli M, Marziliano P, Blu T. Sampling signals with finite rate of innovation [J]. *IEEE Transactions on Signal Processing*, 2002, **50**(6): 1417 – 1428. DOI: 10.1109/TSP.2002.1003065.

[22] Tur R, Eldar Y C, Friedman Z. Innovation rate sampling of pulse streams with application to ultrasound imaging [J]. *IEEE Transactions on Signal Processing*, 2011, **59**(4): 1827 – 1842. DOI: 10.1109/TSP.2011.2105480.

[23] Yang F, Hu J H, Li S Q. A total least squares reconstruction algorithm of UWB signals based on sub-nyquist sampling [J]. *Journal of Electronics & Information Technology*, 2010, **32**(6): 1418 – 1422. DOI: 10.3724/SP.J.1146.2009.00879. (in Chinese)

[24] Urigüen J A, Eldar Y C, Dragotti P L, et al. Sampling at the rate of innovation: Theory and applications [M]// *Compressed Sensing*. Cambridge, UK: Cambridge University Press, 2012: 148 – 209.

[25] Zhang Y, Song L L, Han J F. Research on image fusion and stitching algorithm for UAV aerial images [J]. *Journal of Inner Mongolia University of Technology (Natural Science Edition)*, 2020, **39**(4): 265 – 272. DOI: 10.13785/j.cnki.nmggydxxbzkxb.2020.04.004. (in Chinese)

基于 SoS 核函数调制的超声图像伪影剔除方法

宋寿鹏 贾 慧 陈 丹

(江苏大学机械工程学院, 镇江 212013)

摘要:针对超声图像伪影严重的问题,提出了一种基于 SoS 核函数调制的超声图像伪影剔除方法,该方法能同时剔除由等声程线扩散、传感器拖尾现象和检测噪声产生的伪影.该方法利用 SoS 核函数对测得的超声回波信号进行调制,对调制后的信号等间隔低速率采样来获取离散序列值,再对离散序列进行离散傅里叶变换得到傅里叶系数序列,利用谱估计算法对回波信号参数进行估计,获取检测信号的特征参数,最后对回波信号进行自适应重构,计算声场得到超声图像.试验结果表明,聚焦和直探头对槽和通孔类缺陷的去伪影效果明显,与传统 B 扫图像相比,峰值信噪比分别达到了 24.306、23.213、15.074 和 16.444 dB,结构相似度分别为 0.931、0.932、0.746 和 0.773,表明该算法有效提高了缺陷图像的质量.

关键词:无损检测;超声图像;伪影;SoS 核函数;缺陷

中图分类号:TH878